Solid Freeform Fabrication 2018: Proceedings of the 29th Annual International Solid Freeform Fabrication Symposium – An Additive Manufacturing Conference
Reviewed Paper

FINITE ELEMENT MODELING OF METAL LATTICES USING COMMERCIAL FEA PLATFORMS

E. Arrieta *, Jorge Mireles*, C. Stewart*, C. Carrasco*, and R. Wicker*

*The University of Texas at El Paso, El Paso, TX, 79968

Abstract

The introduction of geometrical features into standard solids result in cellular materials with unique performances. The deformation mechanisms originated by the introduced geometry may not be entirely captured by the current commercial FEM software; resulting in inaccuracies in predicting the performance of cellular metals. Additionally, the inconsistency of AM material properties will result in material models with uncertainty, thus, contributing to the inaccuracy of simulations. The present work shows a process for modeling the strength of EBM Ti-6Al-4V lattices structures; starting from the definition of the convenient experiments to generate the data for the development of material models at different orientation and finalizes with the assignment of these material models to the lattice FEMs. MSC Patran/Nastran is used in this work. Experimental results of the compressive strength of lattice structures are compared with those from the FEM utilizing the different material models created from the experiments.

Keywords: Lattices structures, Ti-6Al-4V, EBM, FEA, DIC

Introduction

Lattice structures typically are more damage tolerant, displaying more uniform mechanical properties in comparison to stochastic foams [1]. Numerical models suggest that latticed materials are more tolerant to defects compared to foams. By randomly removing struts, the modulus and compressive strength of open-cell foams decreased more rapidly than for lattices. Although varied results are reported, investigations coincide in the proportionality of the elastic modulus to density of open-cell materials [2]; thus in regards to damage sensitivity, the removal of struts reduces the modulus in a faster manner than the thinning of these [3]. Well-designed sandwich plates with cellular lattices in the core showed to withstand larger blast impulses than solid plates of the same material and weight [4]. Other investigations with sandwich panels revealed the post-yield response under dynamic loads to be insensitive to the low velocity range of impact; furthermore, a more localized deformation was observed for high velocities. In underwater explosion tests, lattices were found to crush in a progressive manner by a subsequent buckling of struts layers, providing insights as to the effects of filling materials in enhancing plastic deformation of the metal [5]. Thus, for the particular interest of energy absorption applications exposed herein, lattices are selected as better alternatives than foams. Additionally, these non-stochastic architectures have been reported to behave within the characteristic parameters for cellular solids defined in [6], such as slenderness, aspect ratio, relative density and modulus among others [7].

Expressed as the rate of the externally applied energy divided by the amount of mass of the material withstanding it, the normalized absorbed energy is the common parameter to evaluate the capability of materials to dissipate energy. Empirical evidence reports that the bending of struts, the formation and manipulation of multiple shear bands, and microcracking of the constituent material among many other features, also contribute to the absorption of energy [4].
As more applications are developed to use these materials as energy absorbers, structurally efficient members, or a combination of applications, experimental testing of these materials has become a significant component of their development and study. Experimental testing demands valuable resources; numerical simulations ease the bridging from materials science into engineering applications and increase the chances of early experimental success. The development of computer models of cellular materials grants us the availability to modify features on their design and explore their response; all in the same CAD model from which the components will be fabricated by AM.

In this context, this work presents the development of material data sets and finite element models of different lattice materials for comparison with experiments of actual lattice structures under compression. The CAD models were developed in Solidworks, while Patran and Nastran from MSC Software were utilized for the development of FEM and FEA respectively.

Materials and Methods

All the specimens were fabricated with EBM Ti-6Al-4V in an Arcam A2 system. The specimens for testing and comparison with their computer models consisted of two types of lattices: hexagonal unit-cells and reentrant hexagonal unit-cell. Each type of lattice was designed at three different densities from varying the cell size (5mm, 6mm and 7mm) and with length, width and height equal to 5 unit-cells in each direction and the microstruts were 0.8mm x 0.8mm (Figure 1). A monolithic plate was fabricated as part of the lattices, for uniform stress distribution. Three specimens of each density were tested and results averaged. The lattices were tested as per ASTM E9 at a constant cross-head speed equivalent to a strain rate of 0.003 mm/mm · min [8]; (Table 1) in addition, relative densities (ρ*) were calculated by weighting the specimens and subtracting the volume of the plates assuming to have the same density as solid ASTM E9 specimens fabricated and discussed later in this work. The actual lattices and their computer models were compared based on compressive strength.

Table 1 Average compressive properties of lattices.

Lattice	ρ* *(gr/cm3)*	E *(GPa)*	Ultimate Strength *(kPa)*	Specific Strength *(kN*m/kg)*	Specific Modulus *E6(m2/s2)*
5mm HEX, 0.8mm strut	0.800	2.672	40,000	50.000	3.340
6mm HEX, 0.8mm strut	0.600	0.943	21,000	35.000	1.572
7mm HEX, 0.8mm strut	0.470	0.795	15,000	31.915	1.691
5mm RE-HEX, 0.8mm strut	1.130	1.500	35,000	30.973	1.327
6mm RE-HEX, 0.8mm strut	0.820	1.042	21,000	25.610	1.271
7mm RE-HEX, 0.8mm strut	0.650	0.786	13,000	20.000	1.209

The elastoplastic constituent material models were created from stress-strain curves and mechanical properties obtained from testing microstruts and ASTM standards solid specimens printed at different orientations (Figure 2); strain measurements of the specimens were performed by Digital Image Correlation (DIC). Experiments showed similar responses for solid Ti-6Al-4V under compression (ASTM E9) and under tension (ASTM E8). In this manner, the material data set consisted of stress-strain curves and mechanical properties measured on ASTM specimens built at 0º, 30º, 60º and 90º [9], in addition to curves and properties measured on individual microstruts, which form the lattices, built at 0º, 30º, 45 º, 60º and 90º. In this context, the material data set permits assigning material properties to finite elements oriented accordingly; for example, the material models generated from testing 30º specimens (ASTM or microstruts) were assigned only to the finite elements in the 30º microstruts; while 90º properties were assigned to the finite elements in the 90º microstruts, in the computer model. The lattices in this study had microstruts oriented at 90º and 30º only, while the bearing plates were modeled with material properties from ASTM E9 on 90º specimens.

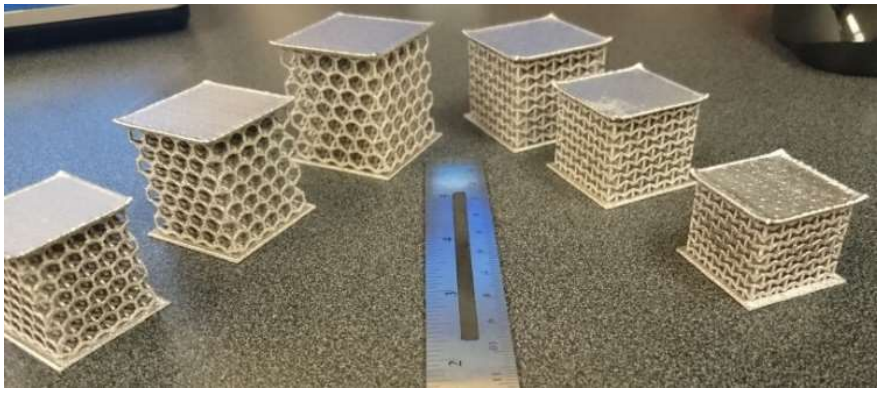

Figure 1 As-fabricated hexagonal (left) and reentrant hexagonal lattices at different densities.

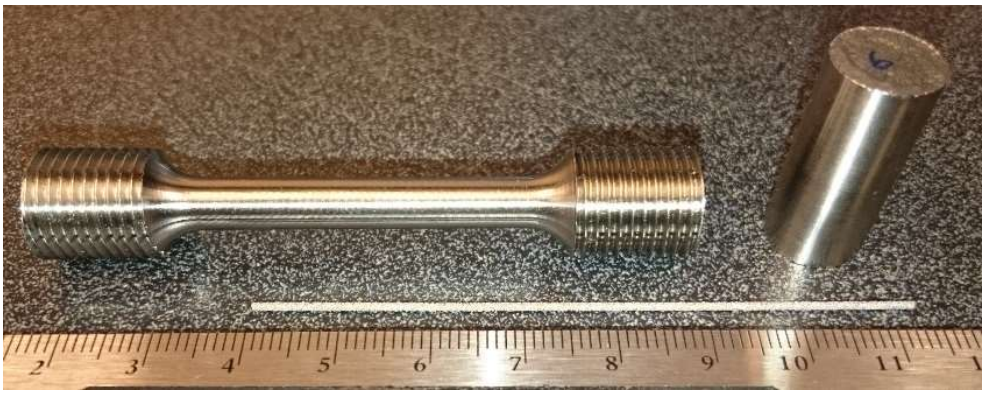

Figure 2 EBM Ti-6Al-4V specimens for testing and determination of material properties.

Finite Element Model

The rapid prototyping process started with the 3D-solid CAD designing of the proposed lattices in Solidworks from Dassault Systèmes. This CAD served as the root file, from where the stereolithography (.stl) and the parasolid (.x_t) format files were exported for fabrication and FEM in the ARCAM A2 system and Patran software respectively. The FEM started with importing the .x_t file into MSC Patran, at the correct scale and required tolerance of dimensions (0.01). Three different conditions were observed in the model: solid bearing plates fabricated at 90°, and microstruts fabricated at 90° and 30°; therefore, three different materials were created in the FEM. The load distribution plates were defined as bulk Ti-6Al-4V, fabricated at 90° whose mechanical properties from the experiments were determined as isotropic with E=113GPa and $\upsilon = 0.33$. The vertical microstruts were defined as 90° microstrut Ti-6Al-4V, whose mechanical properties from the tensile experiments on microstruts at 90° were determined as isotropic with E=113GPa and $\upsilon = 0.33$. The inclined microstruts were defined as 30° microstrut Ti-6Al-4V, whose mechanical properties from the tensile experiments on microstruts at 30° were determined as isotropic with E=104GPa and $\upsilon = 0.31$. The linear elastic and elastoplastic constitutive models were set for both microstrut Ti-6Al-4V properties, whereas for the bulk Ti-6Al-4V only the linear elastic model was set, given the expected strain distribution throughout the lattice. The elastoplastic constitutive models were defined by data fields extracted from averaging the stress-strain curves from the actual experiments (Figure 3). Additionally, the lattices were modeled with material properties from the ASTM E8 standard tension tests, and from the tension test on microstruts.

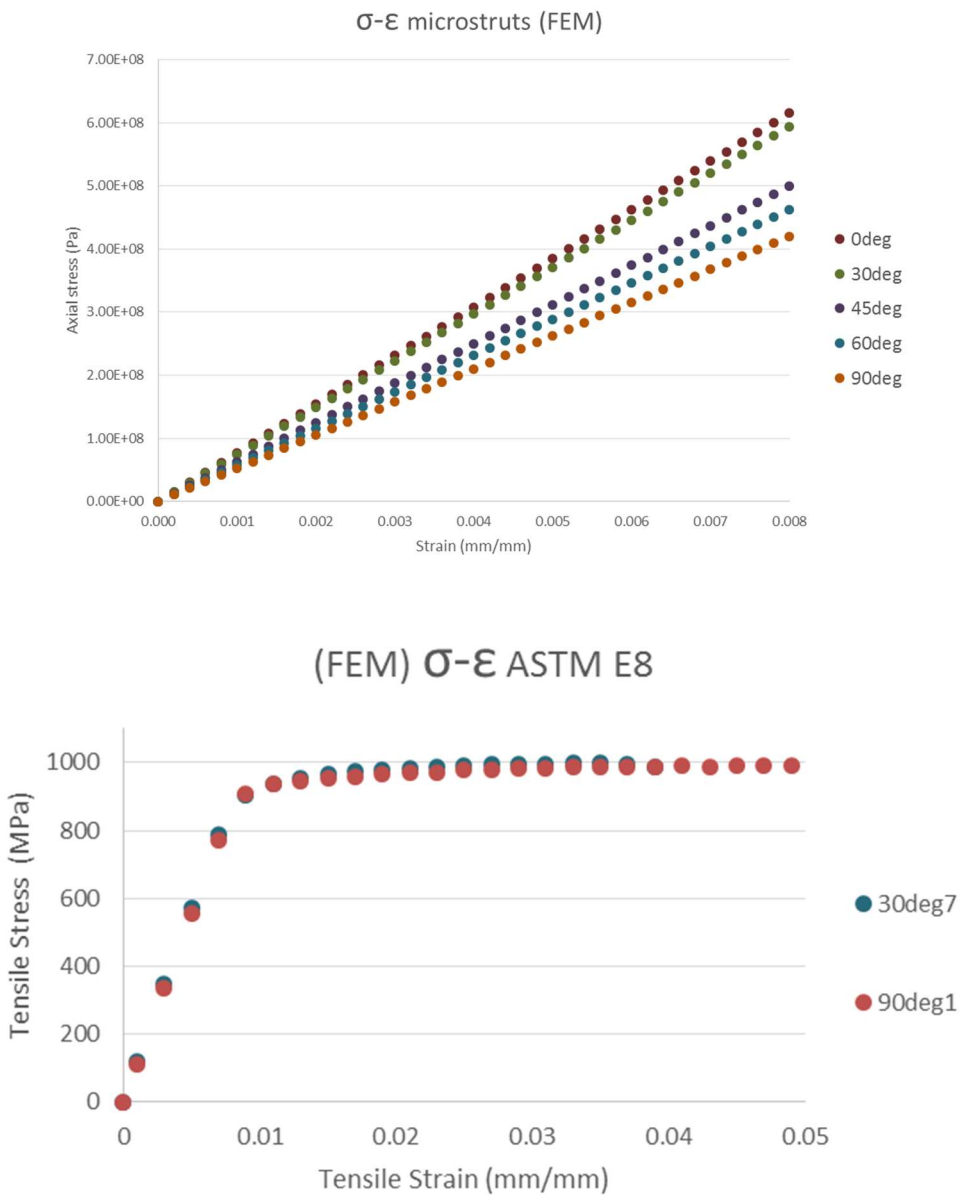

Figure 3 Stress-strain data field used in the material numerical models of microstrut properties (top) and ASTM properties (bottom). These data fields were discretized from actual measured curves. For clarity, only 30° and 90° ASTM E8 are shown. Series names indicate the build angle and last digit as a unique specimen ID

Defining T1, T2, and T3 as translations along orthogonal axes 1, 2 and 3, also named x, y and z, where x-z denotes the horizontal plane, the nodes in the bottom surface of the solid model were constrained for z displacements; similarly, for rotations around the axes R1, R2 and R3, these nodes at the bottom were also constrained for R1 and R3. Total constraint was applied only to nodes of the element at the center of this surface (Figure 4). The upper surface of the plate at the top was exclusively loaded with the vertical element-uniform displacements, corresponding to the

displacements of the actual plate at the ultimate strengths in the experiments; the displacements were measured by DIC (Table 2).

The complex geometry of the 3D CAD solids representing the lattices restricted the element selection to tetrahedrons; based on the nonlinear response observed during testing, the quadratic 10-node tetrahedron (Tet10) was suggested, because the extra node on its sides derives in quadratic shape functions permitting to better capture the nonlinear behavior observed in the testing.

For the initial simulations, the mesh was automatically generated by the solids mesher TetMesh by MSC Patran. The mesh density is controlled by the global edge length parameter; where the longest edge in the geometry, divided by this parameter defines the number of elements along the edge. TetMesh recognizes the longest edge from the geometry of the solid, automatically determining the global edge length based on the minimum element edge length, which has a default value of 20% of the global edge length, producing elements of acceptable quality. Thus, the global edge length was different for each size of lattice in meshes generated automatically.
As a gauge, that facilitated the measurement of the reaction force of the whole lattice at a single point, an additional multipoint constrain element (MPC-RBE2) collecting all the reaction forces from the surface nodes on the exposed face of the bottom bearing plate was included. The RBE2 is characterized by a relationship purely dependent on nodal displacements, meaning it does not possess neither stiffness, mass, force, nor any other relationship (Figure 4**Error! Reference source not found.**).

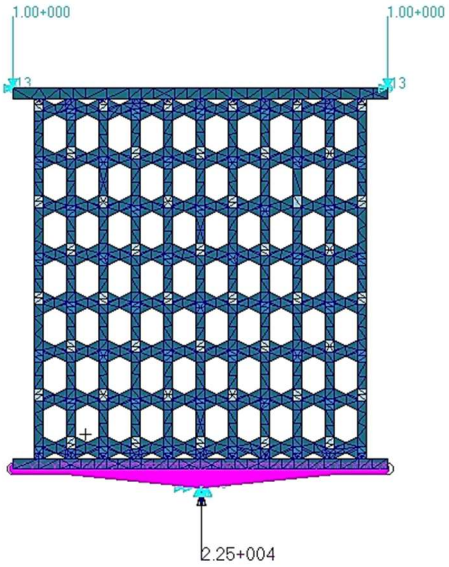

Figure 4 FEM of the hexagonal, 6mm lattice loaded with 1mm element-uniform displacement. MPC and resultant force vector at the bottom.

Finite Element Analysis

The simulations were run in a Dell Precision T5500 computer equipped with Intel Xeon E5603 processor and 6GB DDR3 SDRAM operating at 64-bit. For the solution, the model was divided into four domains with similar number of elements each, and the maximum RAM compromised to solve the model was set at 80%, saving the remaining 20% for the basic operation of the system. The project is solved in Nastran SOL600; a solver for implicit nonlinear solution, following full Newton-Raphson methods with a maximum of 20 iterations per increment, residual force of 0.1 and automatic abort if failed to converge. The adaptive feature is set for defining the loading increments.

Convergence Analysis

Convergence analyses were conducted for all models to ensure that the mesh density was not considerably affecting the results. Four different mesh densities were explored for each of the models representing each of the lattices. One of the densities was the one produced by TetMesh. Given that the mesher takes into consideration the longest edge in the geometry, the mesh refinement controlled by the global edge length (longest geometrical/number of elements) would prioritize the bearing plates. A more effective way to properly size the mesh in these solids was found to define and control the separation of mesh seeds along the edges of the microstruts, in other words, adding more elements where the stress is distributed.

The convergence analysis compared the resultant force at the RBE2 element, produced from applying the displacements at the ultimate strength in the experiments, with the number of elements in the model. Starting at about 70,000 elements, the convergence curves showed a tendency to consistent results. In regards to the computational work, the models started to be significantly more expensive around the 100,000 elements, where the relative efficiency (number of elements / wall time) escalated with no significant change in the resultant force (Table 2 and Figure 5). Thus, the mesh seeding along the microstruts was demonstrated as an effective way for the mesh refinement, and that the consistency of the results may be acceptable in the range of 70,000 to 100,000 elements, when the computational work becomes considerably more expensive.

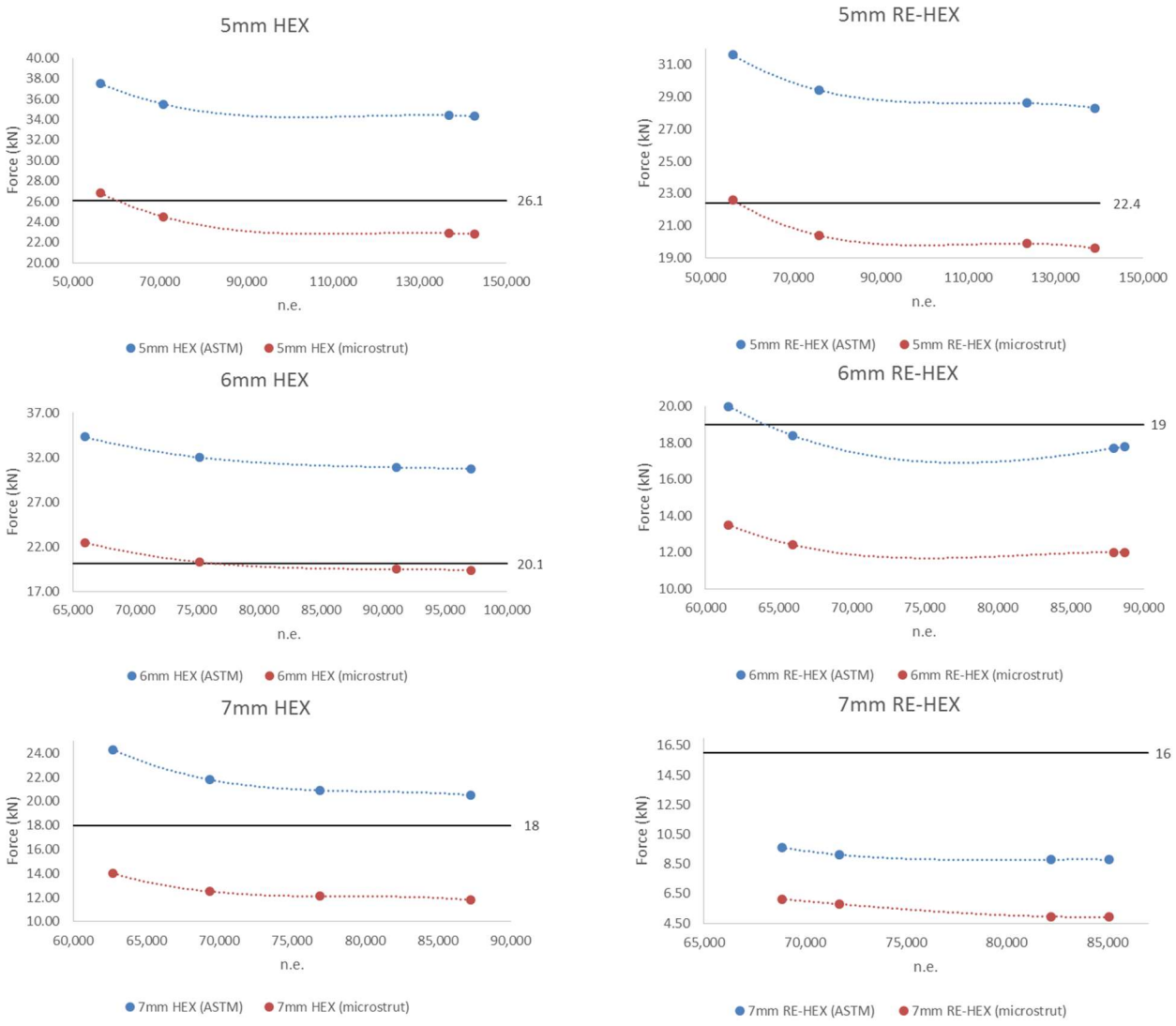

Figure 5 Mesh convergence curves for hexagonal (left) and reentrant hexagonal (right) models. 5mm, 6mm and 7mm unit-cell sizes (top to bottom); two material properties per graph are shown. Solid line representing the experimental average ultimate load.

Results and Discussion

The results of the analyses were evaluated by comparing the nodal force reaction from the independent node at the RBE2 element and the average ultimate force from the experiments. The models were created in two variants: one using the material properties data from the ASTM E8 tests, and another with the data from the tension tests of microstruts (Figure 3).

In general, the models displayed very uniformly distributed stress fields throughout the latticed region, suggesting an efficient energy-distributing material (Figure 6). The models also

indicated that inclined microstruts absorb most of the loading, thus it is advisable to optimize them for an increased capacity (Figure 7). The 90° microstruts showed a lower stress among both configurations, however, the reentrant hexagonal lattices presented columns with lower stresses than the hexagonal. These conditions are the result of the purely compressive state in the hexagonal cells compared to the combination of inclined microstruts in tension and columns under compression in the reentrant hexagonal lattice (Figure 8). It was observed that, by extending the compressive forces to the columns, the purely compressive state better distributed the stresses to more material, compared to the stress distribution at the nodes in the reentrant hexagonal lattices (Figure 9). This more uniform stress distribution by the hexagonal unit-cells explains the failure at lower loads of the reentrant hexagonal lattices that concentrates most of the stress in the inclined microstruts under tension (Figure 10). In similar manner, the inclined microstruts are observed to support most of the shear stress (Figure 11). It is important to be aware that, because of the fragility of the Ti-6Al-4V, the reentrant unit-cells failed before completely developing its negative Poisson effect, and before the cells reconfigured for a second, purely compressive, loading stage that might result in stronger materials with the same amount of mass.

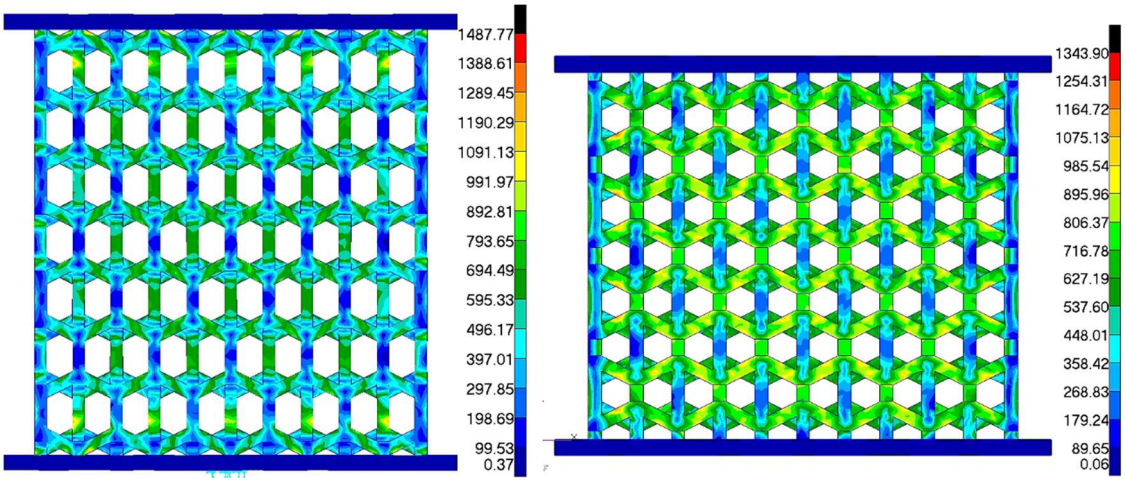

Figure 6 von Mises stress distribution (MPa) in hexagonal (left) and reentrant hexagonal (right) 5mm lattices. Darker colors indicate lower stress.

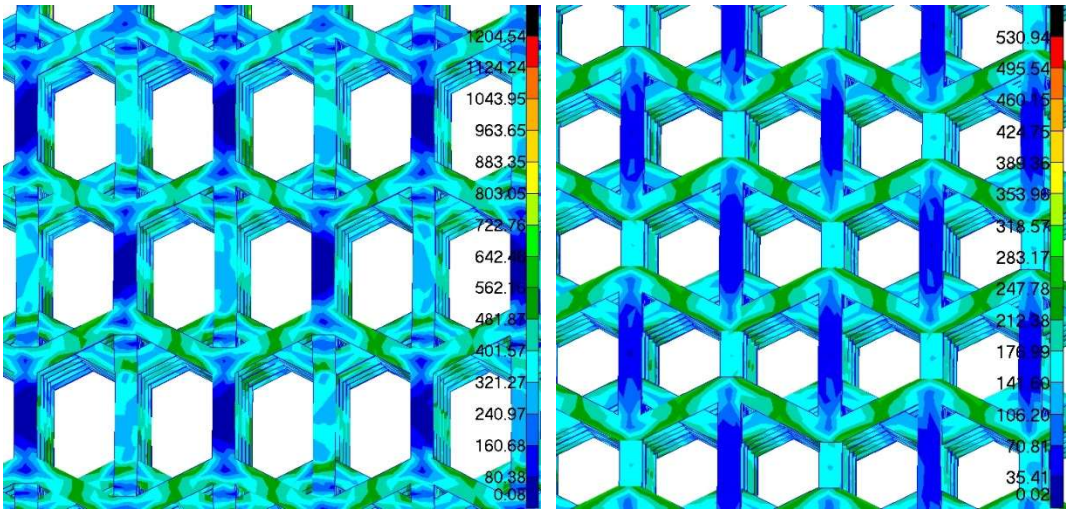

Figure 7 Inclined microstruts with higher von Mises stress (MPa).

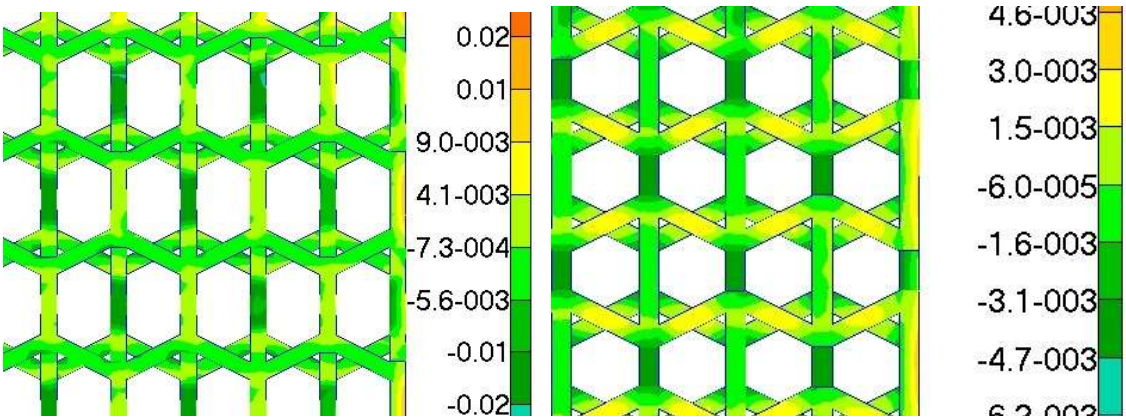

Figure 8 Stress "Y" component in MPa; purely compressive stress state in 7mm hexagonal lattices (left). Tension (-) and compression (+) stresses in 7mm reentrant lattices (left).

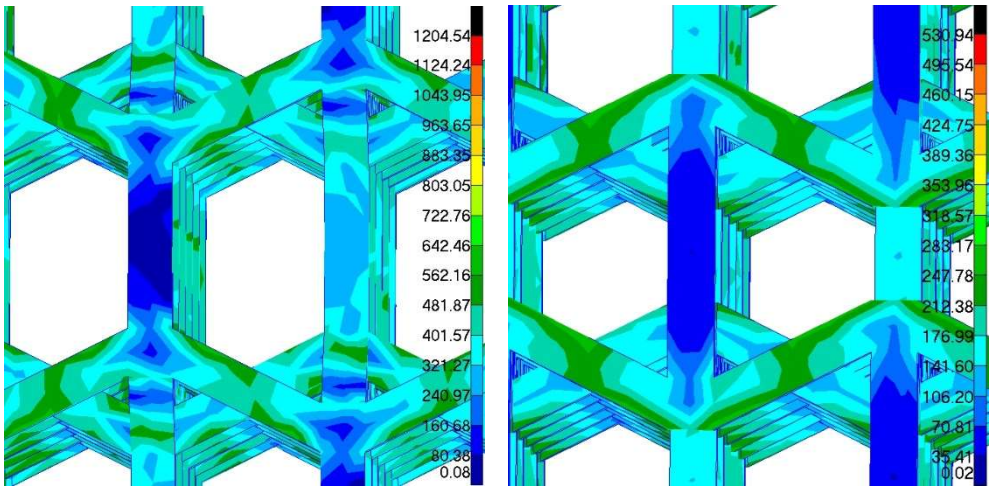

Figure 9 Stressed microstruts and low-stress columns in reentrant hexagonal lattices. Columns in hexagonal lattices dispersing compressive stresses from microstruts (left).

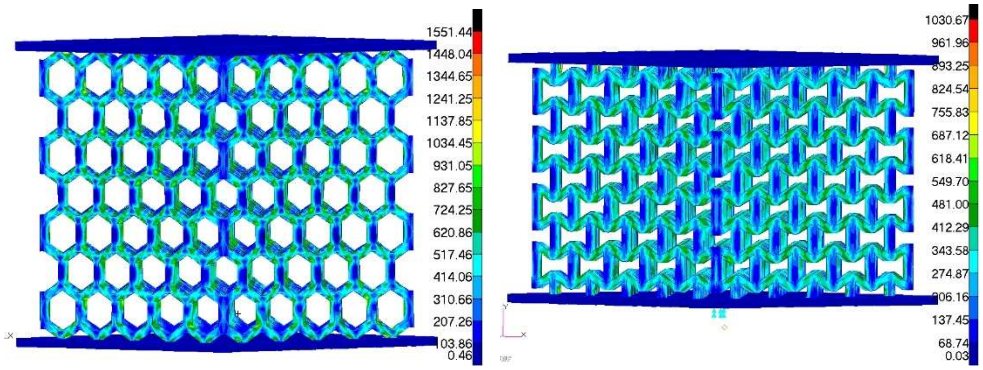

Figure 10 Dimetric of 6mm lattices displaying von Mises stress distribution (MPa).

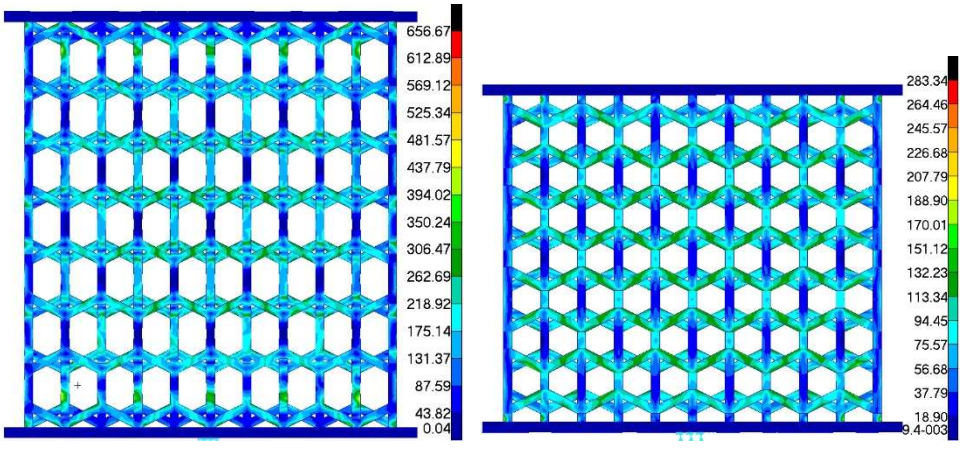

Figure 11 Shear stress distribution in 7mm lattices (MPa).

Although the models exhibited convergence, demonstrating that results stabilize with denser meshes, not all the models showed accuracy in predicting the experimental results (Table 2). The hexagonal lattice models, with material properties from the experimental data from testing microstruts, displayed resultant forces (at the RBE2) closer to the average experimentally obtained values. On the other hand, results from the reentrant hexagonal lattices showed closer values to the experimental results, when the material properties input data derived from the standard tension tests. On the comparison of material properties, the models with material properties developed from the microstrut tests showed to be more accurate than using data from standard tension tests, this could be explained from the larger sensitivity to manufacturing defects of the microstruts, adding uncertainty; besides the removal of surface defects in ASTM E8 specimens. On the comparison of the selected geometry; the hexagonal geometries exhibited values closer to the experimental results, when compared to the reentrant hexagonal, this could be caused by the more complex stress distribution subjected to tension and compression in the reentrant hexagons, compared to the purely-compressive stress state in the hexagonal lattice. On the comparison of the size of the unit-cell; the smallest size (5mm), the models showed more accurate predictions; this, given the increased density of the lattice diminishing the geometrical nonlinearities introduced at the mesoscale, in other words, the smaller the unit-cell, the denser the lattice, and the closer of this to uniformly behave as a standard solid.

The two unit-cell configurations displayed more uniformly distributed plastic strain fields for larger unit-cell sizes (Figure 12). Another interesting, and expected, feature in the models is that the largest strains developed in the microstuts in the interior of the lattice (Figure 13). The reentrant hexagonal lattice models were also capable of developing the negative Poisson effect (Figure 14) and measured in [8]; suggesting an additional argument favoring the confidence on the FEM for evaluating the auxetic deformation mechanisms, and therefore the strain field distribution, in other words, the deformation mechanisms in the models were similar to those from the experiments.

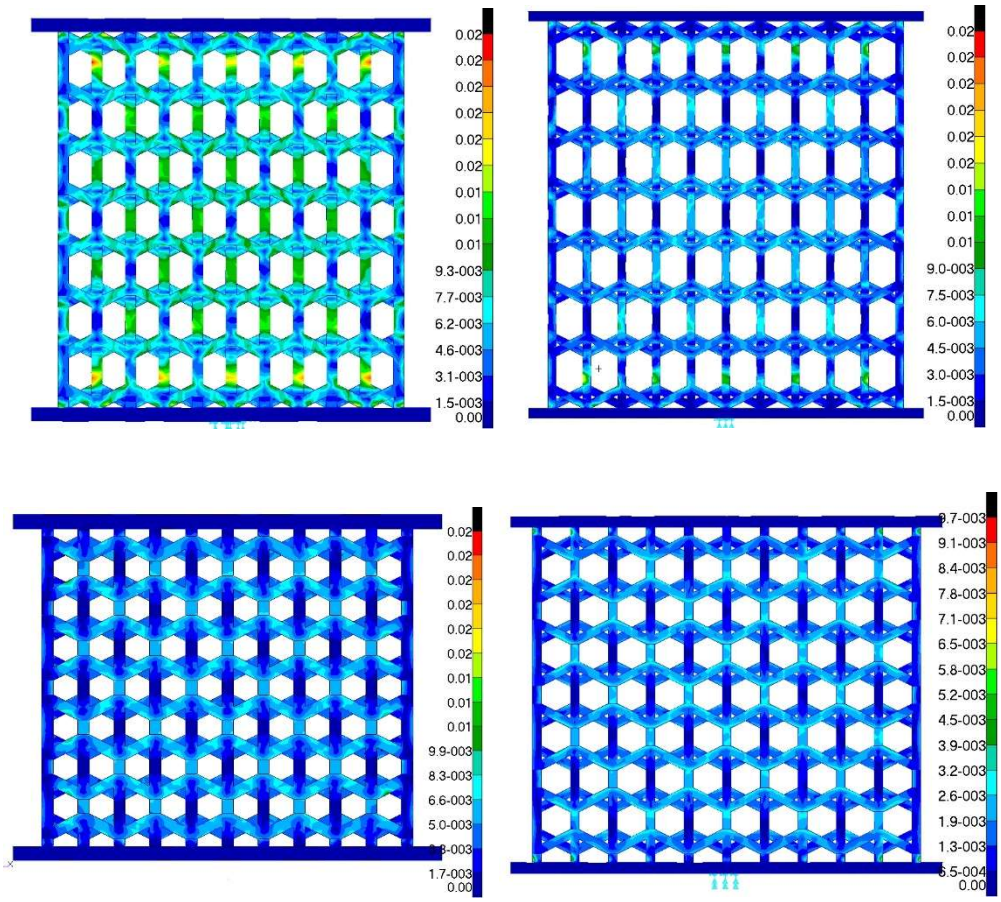

Figure 12 von Mises plastic strain hexagonal (top) and reentrant hexagonal (bottom) lattices with 5mm (left) and 7mm (right) unit-cells.

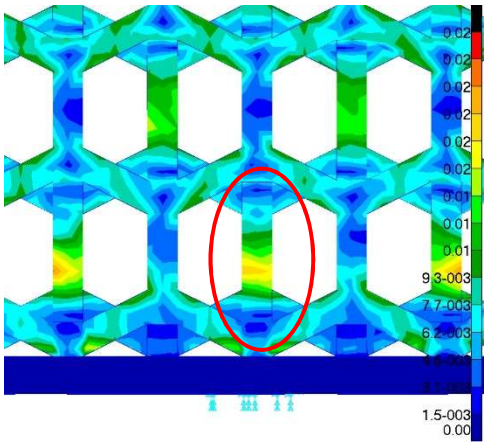

Figure 13 Plastic strain in interior microstruts.

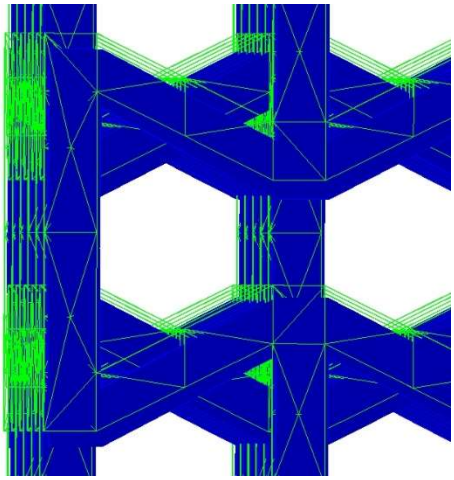

Figure 14 Undeformed model wireframe in highlighted light color on the left side face of the lattice, highlighting the auxetic behavior.

Table 2 Summary of FEMs at different mesh density and material properties

Lattice	Exp.Avg. Ult.Load (kN)	Std.Dev. (kN)	c.o.v.
5mm HEX, 0.8mm strut	26.10	0.70	0.03
6mm HEX, 0.8mm strut	20.10	1.03	0.05
7mm HEX, 0.8mm strut	18.00	0.75	0.04
5mm RE-HEX, 0.8mm strut	22.40	0.50	0.02
6mm RE-HEX, 0.8mm strut	19.00	0.69	0.04
7mm RE-HEX, 0.8mm strut	16.00	1.34	0.08

FEM / Experimental	# of seeds 90° microstruts	# of seeds 30° microstruts	n.e.	Force (kN) *w/std. properties*	% change	Error Vs Exp.	Force (kN) *w/microstrut properties*	% change	Error Vs Exp.	Walltime (s) w/std. properies	% change	Relative efficiency (n.e./s)	Walltime (s) w/microstrut properties	% change	Relative efficiency (n.e./s)
5mm HEX avg.experimental (displ.=0.82mm, F=26.1kN)	auto	auto	56,364	37.50	-	43.68%	26.80	-	2.68%	912	-	61.8	955	-	59.0
	2	2	70,903	35.50	-5.3	36.02%	24.50	-8.6	-6.13%	2,255	147.3	31.4	1,211	26.8	58.5
	2	3	136,761	34.40	-8.3	31.80%	22.90	-14.6	-12.26%	31,318	3334.0	4.4	27,933	2824.9	4.9
	2	3	142,697	34.30	-8.5	31.42%	22.80	-14.9	-12.64%	31,173	3318.1	4.6	29,658	3005.5	4.8
6mm HEX avg.experimental (displ.=1.0mm, F=20.1kN)	auto	auto	65,955	34.30	-	70.65%	22.50	-	11.94%	1,156	-	57.1	1,182	-	55.8
	3	2	75,251	32.00	-6.7	59.20%	20.30	-9.8	1.00%	1,443	24.8	52.1	1,625	37.5	46.3
	2	3	91,101	30.90	-9.9	53.73%	19.50	-13.3	**-2.99%**	2,420	109.3	37.6	2,546	115.4	35.8
	3	3	97,120	30.70	-10.5	52.74%	19.40	-13.8	-3.48%	1,356	17.3	71.6	1,401	18.5	69.3
7mm HEX avg.experimental (displ.=0.9mm, F=18.0kN)	auto	auto	62,726	24.30	-	35.00%	14.00	-	-22.22%	1,000	-	62.7	1,021	-	61.4
	3	2	69,329	21.80	-10.3	21.11%	12.50	-10.7	-30.56%	1,098	9.8	63.1	1,120	9.7	61.9
	2	3	76,907	20.90	-14.0	16.11%	12.10	-13.6	-32.78%	1,375	37.5	55.9	1,228	20.3	62.6
	3	3	87,226	20.50	-15.6	13.89%	11.80	-15.7	-34.44%	3,582	258.2	24.4	3,525	245.2	24.7
5mm RE-HEX avg.experimental (displ.=0.68mm, F=22.4kN)	auto	auto	56,214	31.60	-	41.07%	22.60	-	0.89%	1,197	-	47.0	1,399	-	40.2
	3	2	76,005	29.40	-7.0	31.25%	20.40	-9.7	-8.93%	1,262	5.4	60.2	1,262	-9.8	60.2
	2	3	123,517	28.60	-9.5	27.68%	19.90	-11.9	-11.16%	14,708	1128.7	8.4	14,708	951.3	8.4
	3	3	138,970	28.30	-10.4	26.34%	19.60	-13.3	-12.50%	21,429	1690.2	6.5	21,429	1431.7	6.5
6mm RE-HEX avg.experimental (displ.=0.59mm, F=19.0kN)	auto	auto	61,584	20.00	-	5.26%	13.50	-	-28.95%	705	-	87.4	676	-	91.1
	2	2	65,992	18.40	-8.0	-3.16%	12.40	-8.1	-34.74%	848	20.3	77.8	957	41.6	69.0
	2	3	88,714	17.80	-11.0	**-6.32%**	12.00	-11.1	-36.84%	1,169	65.8	75.9	1,412	108.9	62.8
	3	3	87,944	17.70	-11.5	-6.84%	12.00	-11.1	-36.84%	1,728	145.1	50.9	2,129	214.9	41.3
7mm RE-HEX avg.experimental (displ.=0.38mm, F=16.0kN)	auto	auto	68,858	9.60	-	-40.00%	6.14	-	-61.63%	1,156	-	59.6	1,162	-	59.3
	2	2	71,701	9.13	-4.9	-42.94%	5.80	-5.5	-63.75%	1,116	-3.5	64.2	1,282	10.3	55.9
	3	3	82,183	8.80	-8.3	-45.00%	4.95	-19.4	-69.06%	1,471	27.2	55.9	1,718	47.8	47.8
	2	3	85,062	8.80	-8.3	-45.00%	4.93	-19.7	-69.19%	3,652	215.9	23.3	1,847	59.0	46.1
			Avg.err. (std.prop.)	Avg.err. (microstruts)	Avg.err. (HEX)	Avg.err. (REHEX)	Avg.err. (5mm)	Avg.err. (6mm)	Avg.err. (7mm)						
			32.76%	25.32%	26.60%	31.47%	21.13%	25.18%	41.06%						

Conclusions

Although the complex geometry of the lattices limited the selection of elements to tetrahedrons, the resultant compression force in the FEMs show convergence for mesh refinement.

TetMesh was found not effective in increasing the density of the mesh for this kind of models. A better approach was presented by mesh seeding the edges of the microstruts. Following the mesh seeding approach for the mesh generation, the variation of the results, because the size of the mesh, can be neglected for models over 70,000 elements, but no larger than 100,000, when the computational work dramatically increases.

On the prediction of the experimental compressive forces applied, some models showed considerable errors (up to 70.65%); however, this error needs to be viewed within the context of the variability in the material properties as shown in [8], where the coefficient of variation of the failure loads for microstruts can be as high 0.353. In general; on the selected geometry, the hexagonal models showed more accurate compression forces compared to the reentrant hexagonal. On the material properties used for modeling, the models with input data derived from testing microstruts showed more accurate with an average error of 25.32% in predicting the average experimental force, compared to those with input data from ASTM E8 tests, with an average error of 32.76%. On the unit-cell size, the smallest (5mm) showed more accurate in estimating the experimental compression force. In summary, in predicting the average experimental resultant compression force applied, the model for hexagonal lattices showed to be more accurate, with a 2.99% average error, for the 6mm unit-cell and microstrut properties; whereas the most accurate models for reentrant hexagonal lattices was found with 6mm unit-cell and standard material properties, with an average error of 6.32%.

Recommendations and Future Work.

On the development of more effective automatic meshers; it is recommended that commercial FEM platforms wishing to start modeling cellular lattices, to allow the user to specify the region of interest where the global edge length, as discussed in the convergence analysis, needs to be defined.

On the error of the models predicting the experimental results; it may be advisable to investigate the development of newer technologies for finite elements that allow to capture the nonlinear effects of the geometries introduced at the mesoscale.

On improving the accuracy of the presented models, a more elaborated model with mixed elements could be developed. For example, for mechanistic unit-cells, in regions where high stresses are expected, such as in the nodes of the lattices, elements of higher order are better suited for capturing stress distribution, whereas first order elements may be suitable for the microstruts. However, this could be time consuming, and thus, it might be seen restrictive in rapid prototyping. Although the material properties derived from testing microstruts include the effect of the manufacturing defects, the uncertainty on the properties remains high, because of the size of the microstrut. In that context, and because the nodes of the finite elements are commonly assigned by software in a deterministic manner, the manufacturing defects could also be included in the FEM, by randomly varying the coordinates of the nodes at the free faces of the elements. The

limits for this random variation could be defined by the metrics of the surface defects in microstruts.

Lastly, in further understanding the capabilities and limitations of the commercial FEM/FEM platforms simulating cellular solids with large deformations, it is recommended to evaluate the presented development of these models using more ductile constituent solid such as stainless steel.

Acknowledgments

This work was supported by the W.M. Keck Center for 3D Innovation, and partially funded by the NSF grant #1405526.

References

[1] D. T. Queheillalt and H. N. G. Wadley, "Cellular metal lattices with hollow trusses," *Acta Mater.*, vol. 53, no. 2, pp. 303–313, Jan. 2005.
[2] Y. W. Kwon, R. E. Cooke, and C. Park, "Representative unit-cell models for open-cell metal foams with or without elastic filler," *Mater. Sci. Eng. A*, vol. 343, no. 1–2, pp. 63–70, Feb. 2003.
[3] J. C. Wallach and L. J. Gibson, "Defect sensitivity of a 3D truss material," *Scr. Mater.*, vol. 45, no. 6, pp. 639–644, Sep. 2001.
[4] F. Zhu, G. Lu, D. Ruan, and Z. Wang, "Plastic Deformation, Failure and Energy Absorption of Sandwich Structures with Metallic Cellular Cores," *Int. J. Prot. Struct.*, vol. 1, no. 4, pp. 507–541, Dec. 2010.
[5] P. J. Tan, S. R. Reid, and J. J. Harrigan, "On the dynamic mechanical properties of open-cell metal foams – A re-assessment of the 'simple-shock theory,'" *Int. J. Solids Struct.*, vol. 49, no. 19–20, pp. 2744–2753, Oct. 2012.
[6] Ashby, M. F., Evans, A., Fleck, N.A., Gibson, L.J., Hutchinson, J.W., and Wadley, H.N.G., *Metal Foams - A Design Guide*. Boston: Butterworth-Heinemann, 2000.
[7] K. Ushijima, W. J. Cantwell, R. a. W. Mines, S. Tsopanos, and M. Smith, "An investigation into the compressive properties of stainless steel micro-lattice structures," *J. Sandw. Struct. Mater.*, vol. 13, no. 3, pp. 303–329, May 2011.
[8] E. Arrieta, "Comprehensive finite element modeling of Ti-6Al-4V cellular solids fabricated by electron beam melting," *ETD Collect. Univ. Tex. El Paso*, pp. 1–123, Jan. 2017.
[9] E. Arrieta, M. S. Haque, J. Mireles, C. M. Stewart, C. Carrasco, and R. Wicker, "Mechanical behavior of differently oriented EBM Ti-6Al-4V components using digital image correlation," *J. Eng. Mater. Technol.*, Jun. 2018.